Applied Surface Science 732 (2026) 166511

Contents lists available at ScienceDirect

Applied Surface Science

journal homepage: www.elsevier.com/locate/apsusc

Full length article

Thermodynamic and kinetic properties of 2D carbon selenide for efficient sodium-ion batteries (SIBs)

Talha Zafer [a,b,*], Deobrat Singh [c]

[a] Department of Materials Science and Engineering, Faculty of Mechanical, Maritime and Materials Engineering, Delft University of Technology, Mekelweg 2, Delft, 2628 CD, The Netherlands
[b] Vocational School of Health Services, Sakarya University, 54050, Sakarya, Turkey
[c] Department of Materials Science and Engineering, KTH The Royal Institute of Technology, Stockholm SE, 100 44, Sweden

ARTICLE INFO

Keywords:
Sodium-ion batteries
Carbon selenide
Fast ion diffusion
First-principles calculations
Energy storage

ABSTRACT

Despite the promise of sodium-ion batteries (SIBs) for large-scale energy storage, the development of high-performance anode materials remains a critical challenge. Here, we report that the two-dimensional β-phase carbon selenide (β-CSe) monolayer exhibits remarkable Na-ion storage properties identified through comprehensive first-principles calculations. The buckled honeycomb structure demonstrates exceptional stability with positive phonon frequencies and preserved C-Se bonds during molecular dynamics at both room temperature (300 K) and elevated temperature (400 K). Na adsorption occurs preferentially at hollow sites with strong binding energies (−2.95 eV on C-side) and substantial charge transfer (0.82|e|), thermodynamically favoring uniform Na distribution which may help suppress dendrite formation. Strikingly, the material exhibits ultra-facile Na diffusion with maximum energy barriers of only 0.019-0.021 eV, among the lowest reported for SIB anodes, suggesting exceptional rate performance. Basin-hopping Monte Carlo simulations reveal a theoretical capacity of 589 mAh/g with an average insertion potential of 1.11 V, while the material advantageously transitions from semiconductor to metallic behavior upon Na insertion. The anisotropic Poisson's ratio (as low as 0.05) further minimizes volume changes during cycling. These findings establish β-CSe as a promising candidate for high-performance SIB anodes and provide valuable insights for designing advanced battery materials.

1. Introduction

The rapid growth of renewable energy technologies has intensified the demand for efficient and sustainable energy storage systems. Owing to their superior thermodynamic and kinetic properties, including high energy density, favorable insertion potential, and excellent cycling performance, lithium-ion batteries (LIBs) have been extensively integrated into various electronic devices and electric vehicles [1–4]. Despite their continuous performance improvements, which have expanded their applications to both small and large-scale technologies [5–7], widespread implementation of LIBs has been constrained by concerns regarding lithium resource scarcity, geographical concentration of reserves, and associated high costs [8]. Consequently, sodium-ion batteries (SIBs) have emerged as a promising alternative for large-scale energy storage applications, offering significant advantages including abundant sodium resources, cost-effectiveness, high ionic conductivity, and electrochemical properties similar to lithium-based systems [9–13].

Computational materials design, particularly density functional theory (DFT)-based first-principles calculations, has become an indispensable tool for accelerating the discovery and optimization of advanced battery materials. DFT methods enable accurate prediction of key performance metrics including adsorption energetics, diffusion barriers, electronic properties, and structural stability at substantially lower cost and time compared to experimental synthesis and characterization. This computational screening approach has successfully identified numerous promising electrode materials and provided mechanistic insights that guide experimental efforts, making it essential for the rational design of next-generation energy storage systems [14].

While SIBs benefit from similar chemistry to LIBs and can leverage technological advancements in materials and cell design already established for lithium systems [15], their commercialization faces significant challenges, particularly regarding suitable anode materials. Conventional graphite anodes used in LIBs show limited sodium storage

* Corresponding author at: Department of Materials Science and Engineering, Faculty of Mechanical, Maritime and Materials Engineering, Delft University of Technology, Mekelweg 2, Delft, 2628 CD, The Netherlands.
E-mail address: T.Zafer@tudelft.nl (T. Zafer).

https://doi.org/10.1016/j.apsusc.2026.166511
Received 18 December 2025; Received in revised form 16 February 2026; Accepted 2 March 2026
Available online 11 March 2026

capacity due to the larger ionic radius of Na^+ (1.02 Å) compared to Li^+ (0.76 Å), which restricts sodium intercalation [16,17]. Extensive research efforts have been directed towards identifying alternative anode materials specifically designed for SIBs [12,18–21]; however, critical issues such as limited specific capacity and poor cycling stability remain unresolved, hampering their practical implementation. To advance SIB anode development, new materials with enhanced physical and chemical properties must be conceptualized and systematically investigated, with density functional theory and basin-hopping Monte Carlo computations offering powerful approaches for predicting and understanding the thermodynamic and kinetic characteristics of potential candidates [4,22–26].

Two-dimensional (2D) materials present particularly promising characteristics as negative electrodes for energy storage applications, offering distinct advantages over their bulk counterparts [27–29]. Recent research has focused on layered group-IV and VI compounds with structures analogous to black phosphorene (α-P) and blue phosphorene (β-P), which have been both theoretically predicted and experimentally synthesized, demonstrating significant potential for optoelectronic, photovoltaic, sensing, and battery applications [30,31]. The buckled configuration of these materials, resembling blue phosphorene, typically generates intrinsic dipoles arising from electronegativity differences between constituent atoms in the top and bottom layers. Computational studies of Si, Ge, and Sn monochalcogenides (SiS, SiSe, GeS, GeSe, SnS, and SnSe) have revealed their exceptional capacity for handling rapid charge/discharge processes in both lithium and non-lithium ion batteries [32–35].

Inspired by these findings and motivated by the remarkable structural integrity, mechanical strength, and physicochemical properties of carbon selenide, we have systematically investigated the potential of 2D β-CSe as an anode material for sodium-ion batteries. Through comprehensive computational techniques including density functional theory (DFT), ab initio molecular dynamics (AIMD), nudged elastic band (NEB) method, and basin-hopping Monte Carlo (BHMC) algorithm, we first establish the structural, dynamical, and thermal stability of the β-CSe monolayer. We then evaluate Na-binding strengths at various adsorption sites on the β-CSe surface using both standard DFT and DFT-D2 approaches. The insertion potential and theoretical specific capacity are determined through BHMC simulations examining Na-concentration effects on both sides of the β-CSe surface. Additionally, we investigate dilute Na-diffusion pathways along different directions and analyze the structural and electronic properties of the material under mechanical strain and applied transverse electric fields. Compared to other reported 2D materials proposed as battery electrodes, our findings indicate that the β-CSe monolayer represents a highly promising candidate for next-generation sodium-ion battery anodes, offering an exciting addition to the class of materials being considered for advanced energy storage applications.

2. Computational frameworks

2.1. Density functional theory

All structural optimizations and electronic, thermodynamic, and kinetic property calculations were performed within the density functional theory (DFT) framework using the Vienna *Ab Initio* Simulation Package (VASP) [36]. The Perdew–Burke–Ernzerhof (PBE) formulation of the generalized gradient approximation (GGA) [37] was employed self-consistently with the projector augmented wave (PAW) method. Calculations were performed using a plane-wave basis set with a kinetic energy cutoff of 500 eV. Electronic self-consistent energy and force convergence criteria during geometry relaxations were set to 10^{-6} eV and 10^{-3} eV/Å, respectively, using the conjugate-gradient algorithm. To accurately account for van der Waals interactions during Na adsorption, Grimme's semi-empirical dispersion correction (DFT-D2) was applied. We employed the Grimme D2 dispersion correction to account for van der Waals interactions, which has been widely validated for similar 2D materials including phosphorene and chalcogenides. The choice of DFT-D2/D3 over alternative vdW methods (such as optB88-vdW or SCAN+rVV10) was motivated by: (i) computational efficiency enabling the extensive configurational sampling required for BHMC, (ii) established validation for alkali metal adsorption on 2D materials with good agreement to higher-level methods for relative energetics, and (iii) consistency with methodology used in literature studies of comparable materials, facilitating direct comparison of results. To verify the robustness of our results, we performed comparative calculations using DFT-D3(BJ) correction for selected configurations. The comparison confirms that while DFT-D2 produces slightly stronger binding (as expected from its known overbinding tendency), the relative energetic trends including site preferences and diffusion pathway ordering are preserved between both methods, validating our conclusions (Table S1). Quantitative comparison of DFT-D2 and DFT-D3(BJ) results for the fully sodiated Na_2CSe structure is provided in Table S1 of the Supplementary Information. For more precise determination of electronic properties and bandgap values, the Heyd–Scuseria–Ernzerhof (HSE06) hybrid functional with a standard mixing parameter of 25% [38] was used for band structure calculations.

The β-CSe monolayer was modeled using a $(3 \times 3 \times 1)$ supercell with periodic boundary conditions in the x- and y-directions, and a vacuum space of 20 Å along the z-direction to prevent interactions between periodic images. This supercell size provides Na–Na separations exceeding 9 Å in the dilute limit, sufficient to minimize artificial periodic image interactions for single-atom adsorption and diffusion barrier calculations. This supercell dimension is consistent with numerous published studies on 2D anode materials, enabling direct comparison with literature values. Brillouin zone sampling was performed using a Monkhorst–Pack k-point grid of $9 \times 9 \times 1$ for both pristine β-CSe and Na-adsorbed systems [39]. Charge transfer between Na atoms and the β-CSe surface was evaluated using Bader charge analysis [40]. All reported adsorption energies, diffusion barriers, adsorption heights, and charge transfer values were obtained using DFT-D2, as van der Waals corrections are essential for accurate Na adsorption energetics.

To verify the thermal stability of the free-standing β-CSe monolayer after optimization and the reversibility of the electrode after Na-ion removal, we performed *ab initio* molecular dynamics (AIMD) simulations in the NVT ensemble with a time step of 2 fs for 10 ps at room temperature [41,42]. Additional AIMD simulations were performed at 400 K to verify thermal stability at elevated temperatures relevant to battery operating conditions. Phonon dispersion calculations were carried out using the Phonopy code with the PBE-GGA functional to confirm dynamical stability.

The anisotropic mechanical properties of β-CSe were characterized through the directional dependence of Young's modulus and Poisson's ratio. For an anisotropic 2D material, these properties as functions of direction θ relative to the positive x-axis can be expressed as:

$$E(\theta) = \frac{C_{11}C_{22} - C_{12}^2}{C_{11}\sin^4\theta + C_{22}\cos^4\theta + \left(\frac{C_{11}C_{22}-C_{12}^2}{C_{44}} - 2C_{12}\right)\cos^2\theta\sin^2\theta} \quad (1)$$

$$\nu(\theta) = \frac{\left(C_{11} + C_{22} - \frac{C_{11}C_{22}-C_{12}^2}{C_{44}}\right)\cos^2\theta\sin^2\theta - C_{12}(\cos^4\theta + \sin^4\theta)}{C_{11}\sin^4\theta + C_{22}\cos^4\theta + \left(\frac{C_{11}C_{22}-C_{12}^2}{C_{44}} - 2C_{12}\right)\cos^2\theta\sin^2\theta} \quad (2)$$

The Na-ion diffusion pathways and associated energy barriers were investigated using the climbing image nudged elastic band (CI-NEB) method [43], which generates a series of intermediate configurations between specified initial and final positions through linear interpolation and minimizes the energy along the diffusion pathway.

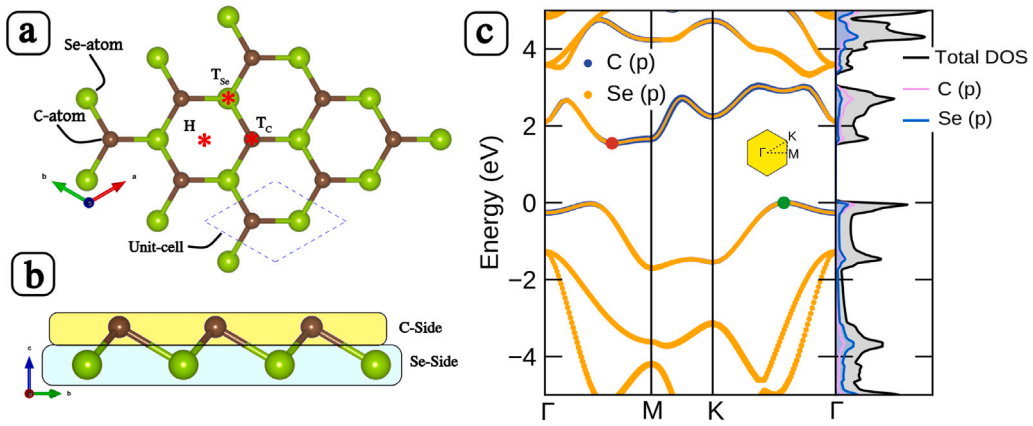

Fig. 1. (a,b) The top and side view of the fully optimized structure of 2D β-phase CSe monolayer, respectively. The unit-cell are marked with black dotted line. The available binding site are marked by red star. (c) The electronic projected band structure and corresponding decomposed density of states of pristine 2D CSe monolayer. The indirect bandgap of 1.544 eV (PBE) is indicated by red and green dots; HSE06 calculations yield a bandgap of 2.1 eV.

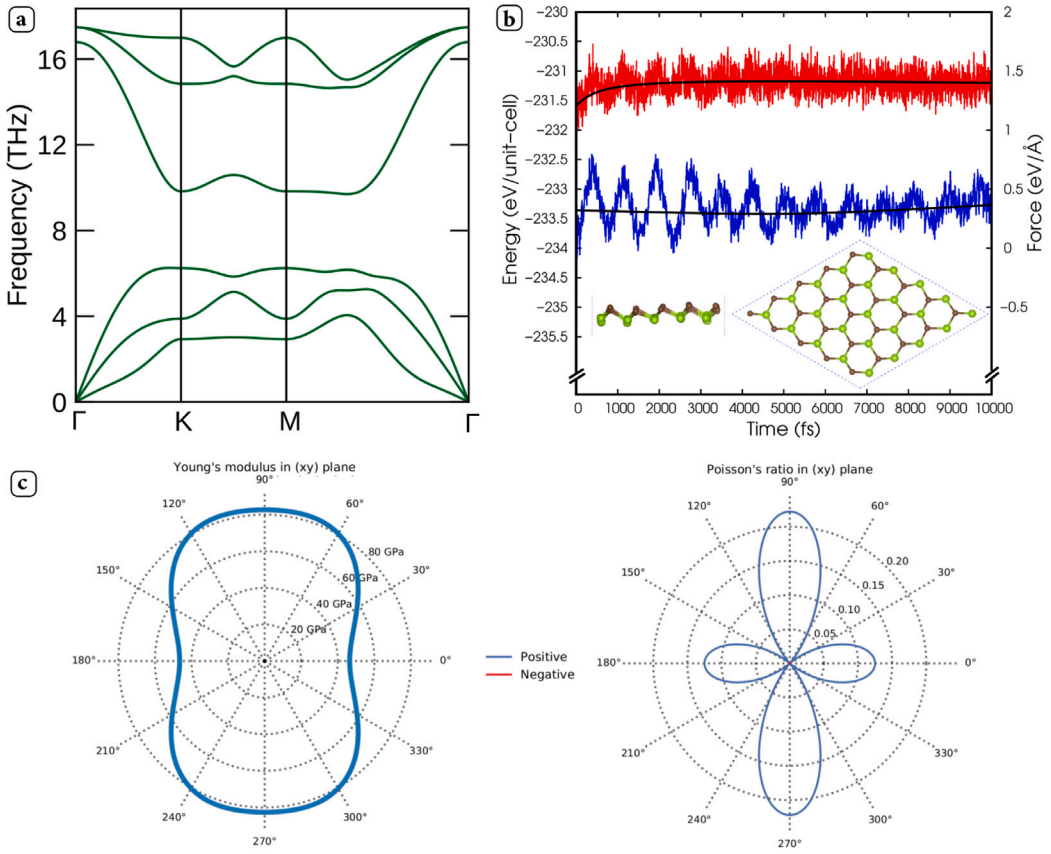

Fig. 2. (a) Phonon dispersion profile of 2D β-phase CSe monolayer, (b) Ab-initio molecular dynamics simulations at room temperature for 10 ps of β-CSe structure, (c) Young's modulus and Poisson's ratio of pristine β-CSe monolayer.

2.2. Basin-hopping Monte Carlo algorithm

3. Results and discussion

3.1. Structural, stability and electronic properties of β-CSe

Firstly, it is quite interesting to get a clear overview of structural, stability and electronic properties of the material before exploring further its possible applications for SIBs. The β-CSe monolayer belongs to the P3m1 space group and is characterized by a unit-cell of one C-atom and Se-atom generating a honeycomb like buckled phase structure as depicted in Fig. 1(a and b). The optimized lattice constant of β-CSe is about a = b = 3.065 Å, which is in good accordance with previous reported studies [44–46].

The bond length (2.055 Å) and buckling thickness (1.045 Å) of the β-CSe monolayer are notably smaller than those of blue phosphorus (β-P), which exhibits a P–P bond length of 2.27 Å and buckling height of 1.24 Å [47]. These shorter bond lengths in β-CSe indicate stronger covalent interactions between C and Se atoms compared to the P–P bonds in β-P. Blue phosphorene (β-P), which shares the buckled honeycomb structure, has been synthesized via molecular beam epitaxy [48]. Buckled silicene has been achieved via epitaxial growth [49]. Given

that β-P has been extensively investigated theoretically and successfully synthesized experimentally through liquid exfoliation and chemical vapor deposition methods, we anticipate that the β-CSe monolayer, with its comparable buckled honeycomb structure but stronger bonding, can be synthesized using similar experimental setups and cell designs, potentially with even better structural stability.

The projected band-structure and total/projected density of states for 2D β-CSe monolayer were computed as given in Fig. 1(c). The band structure were studied along the K-Γ-M-K directions. As shown in Fig. 1(c), the β-CSe monolayer exhibits an indirect bandgap semiconductor characteristic with a bandgap of approximately 1.544 eV (PBE-GGA). HSE06 hybrid functional calculations yield a larger bandgap of 2.1 eV, which is more reliable for comparison with experimental measurements. The valence band maximum (VBM) is located between the Γ and M points, while the conduction band minimum (CBM) is situated between the K and Γ points in the Brillouin zone. The indirect nature of the bandgap is beneficial for battery applications as it ensures semiconducting behavior in the pristine state while allowing metallic conductivity upon Na adsorption, as will be discussed later. In PDOS, major peaks are occurred in the valence-band owing to the 5p-orbital of the Se. The partial density of states show that the DOS in the VBM/CBM are mainly contributed by p-orbitals, with a great contribution near Fermi-level from the p-orbital of C-atoms.

To evaluate the dynamical stability of our structure, the phonon spectrum were calculated through the density functional perturbation theory (DFPT), which reflects the collective vibrational mode of all atoms, wherein an acoustic branch denotes the vibration of the original cell, and the optical branch describes the relative vibration of the atoms in the unit-cell. Fig. 2(a) shows the phonon dispersion curves with positive values of frequency, confirming the dynamic stability of β-CSe monolayer. In addition, owing to the buckling of the structure, out-of-plane (ZA) acoustic modes of β-CSe monolayer are coupled with in-plane longitudinal acoustic (LA) and transverse acoustic (TA) modes. The phonon spectrum curves illustrate that the optical branches are well separated from the acoustical branches, as obtained in the case of β-P [47]. In addition, AIMD simulations at room temperature and a time step of 10 ps were carried out to check the thermal stability of the β-CSe monolayer. As illustrated in Fig. 2(b), the chemical bonds of C-Se remain intact without deformation with a small variation in energy and force during the molecular simulation, which confirms the great thermal stability of the structure. Additional AIMD simulations at 400 K (Figure S4) further confirm the thermal stability at elevated temperatures, with no bond breaking observed throughout the 10 ps simulation. Radial distribution functions at 400 K (Figure S5) show sharp C-Se peaks at 2.02 Å, confirming framework integrity, while the evolution of Na–C and Na–Se distances (Figure S6) demonstrates that Na atoms remain at their adsorption sites throughout the simulation.

Moreover, to confirm the mechanical stability of our structure it is worth to mention the values of linear elastic constants, Young modulus and Poisson's ratio of the β-CSe material. The computed elastic constants are C_{11} = 47.463 GPa, C_{22} = 47.811 GPa, C_{12} = 8.023 GPa and C_{44} = 19.876 GPa which suggest strong bonding between the C- and Se- atoms. The mechanical stability is assured through the following criteria: C_{11} >0; C_{22} >0; C_{44} >0; $C_{11}C_{22} > C_{12}^2$. Fig. 2 (c,d) depicts the in-plane Young's modulus and Poisson's ratio of β-CSe structure along different θ angles. As for the in-plane Young's modulus and the Poisson's ratio, they were computed using Eqs. (1) and (2) to be Y = 23.381 GPa and ν = 0.190, respectively for θ = 0, along the zig-zag direction and Y = 80 GPa, ν = 0.05 for θ = 120 along the armchair direction. It can be further noticed that the maximum value of these two constants are reached along θ = 90, where we found a value greater than 80 GPa for the Young's modulus and a value greater than 0.20 for the Poisson's ratio. As a matter of fact, the little Poisson's ratio value of ν = 0.05 along the armchair direction is very appreciated, highlighting the great capacity of β-CSe to hinder the volume deformation when Na-ions are intercalated into the anode material. This could give a certain intuition on how to orient the β-CSe structure when manufacturing the anode material to well exploit the advantage of the little Poisson's ratio value. Contrary to the well-known graphene material, β-CSe is characterized by a non-circular polar diagram, which yields an anisotropic mechanical nature.

Table 1
Single Na-atom adsorption on both side of β-CSe monolayer: average distance (h) from Na-ion to the surface, and charge transfer as well as work function. Positive Q_{Na} values indicate electrons donated from Na to the CSe surface.

	Na on C-Side			Na on Se-Side		
	h (Å)	Q_{Na} (|e|)	WF	h (Å)	Q_{Na} (|e|)	WF
Hollow	2.54	0.82	3.51	2.02	0.79	3.69
Top C	2.31	0.96	3.68	2.84	0.97	3.51
Top Se	2.57	0.97	3.79	2.78	0.98	3.81

3.2. Binding energy of sodium on β-CSe monolayer

The main approach towards understanding the trends in the adsorption energy of one Na-atom consists principally of identifying the highest preferable adsorption site. The three possible adsorption sites on the material surface as illustrated in Fig. 1(a), were explored considering the ground state structures found by the basin hopping algorithm for each Na-inserted. These adsorption sites can be divided into two categories. The first one consists in adding the Na atom above either C-atom (T_C) or Se-atom (T_{Se}). The second consists in inserting the Na atom above the C_3Se_3 hexagon (H site). In addition, based on the structural geometry of β-CSe, it is necessary to put the adsorbed atoms on both sides, namely, C- and Se-side.

The criteria for identifying the appropriate Na-adsorption site is estimated based on the binding energy formula stated above using a 3 × 3 × 1 super-cell in order to avoid the interaction of adjacent Na-atoms:

$$E_b = E_{Na@CSe} - E_{CSe} - E_{Na} \quad (3)$$

where, $E_{Na@CSe}$, E_{CSe}, and E_{Na} denoted the total energy of adsorbed system, substrate, and Na-atom in bulk, respectively. Considering the definition, the lower the E_b, the stronger the interaction between the CSe substrate and Na-adsorbate is.

Within the binding sites examined, it is observed that H-, T_C and T_{Se} sites exhibit a negative lowest binding energy for Na-atom, suggesting the exothermic behavior of the adsorption process. Fig. 3(a,b) depict the calculated binding energy using DFT and DFT-D2 and Table 1 summarizes the binding height (h), charge transfer, and work function for the three stable binding sites. It can be clearly noticed that the H-site exhibits the lowest binding energy of about −2.954 and −0.9189 eV for both C- and Se-Side, respectively. DFT-D3(BJ) validation calculations confirm that while absolute binding energies are slightly weaker with D3 (consistent with known D2 overbinding tendency), the relative site preference ordering and diffusion barrier trends remain unchanged (see Table S1 and discussion therein). By comparing the binding energy of Na-atom on both sides of β-CSe monolayer, it is found that the adsorption of Na-atom on C-side is about twice more stable than on Se-side. These calculated binding energies are greater with respect to the recently reported 2D materials, including h-BP (−0.160 eV) [50,51], h-BAs (−0.312 eV) [29] and borophosphene (−0.160 eV) [52], revealing a fast charging mechanism with a higher binding interaction occurring between β-CSe and Na-atom versus the weak binding to Na-ions in the hexagonal graphene monolayer. More particularly, these results suggest a uniform spread of Na-atoms on the β-CSe surface throughout the intercalation mechanism instead of gathering up to form metal-dendrites, thermodynamically favoring dispersed Na distribution which may help suppress dendrite formation, thus providing a significant benefit in the stability and safety of advanced Na-ion batteries.

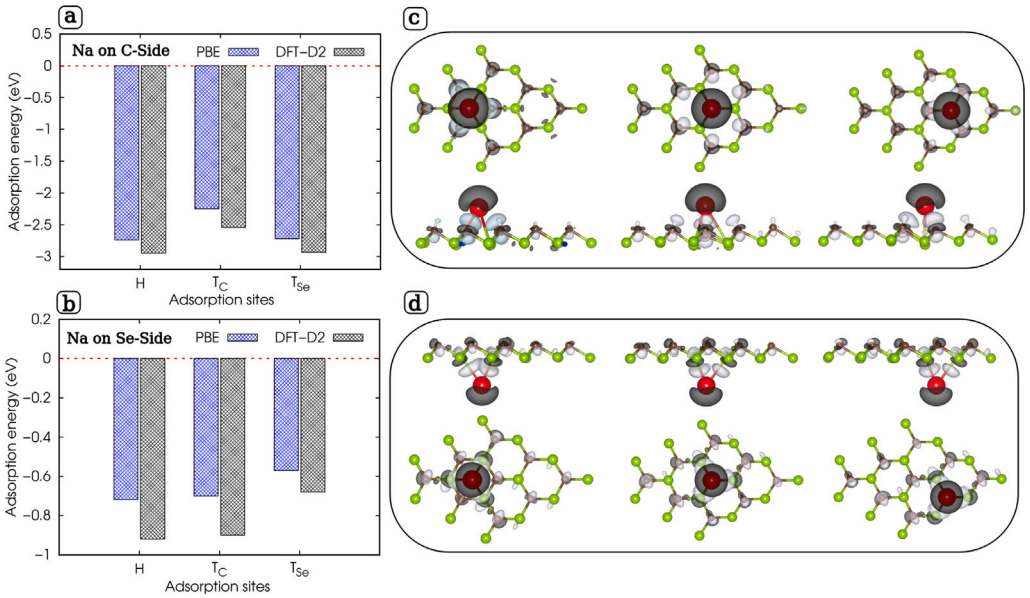

Fig. 3. (a,b) Calculated binding energy of single Na-atom on both side of 2D β-phase CSe monolayer using PBE and DFT-D2 corrections, (c,d) The corresponding computed 3D plot of difference charge density of single Na-ion adsorbed at the most favorable sites. The gray/black denote the electron accumulation/depletion, respectively.

Additionally, the charge transfer values have been estimated for Na-ion adsorbed on the three stable sites of β-CSe surface are tabulated in Table 1 and the corresponding 3D plot of deformed charge density of Na-ion adsorbed at the H-site are illustrated in Fig. 3(c,d). One can clearly notice that Na-ion on both sides behaves as a charge donor which donates 0.82 $|e|$ (C-side) and 0.79 $|e|$ (Se-side) to the β-CSe surface. The Bader charge transfer values between the Na-atom on both sides are in accordance with the computed binding energy depicted in Fig. 3(a,b). The more electrons are transferred by Na-ions to the material surface, the more binding energy is reinforced which shows the Coulomb interaction overwhelms the energetic of the Na-ion adsorption. Comparing the two surfaces (C-side vs. Se-side), we observe that the C-side exhibits both higher charge transfer (0.82 |e|) and stronger binding energy (−2.954 eV) at the hollow site, suggesting that Coulombic interaction plays a significant role in determining the relative binding strengths between the two surfaces. However, when examining different adsorption sites on the same surface, the binding energy is governed not only by charge transfer but also by the local coordination environment and orbital overlap geometry. The hollow site provides optimal three-fold coordination, resulting in stronger binding despite similar charge transfer values to the top sites. This multi-factor nature of the Na-substrate interaction ensures stable adsorption while maintaining the structural integrity of the β-CSe monolayer.

3.3. Equilibrium voltage and theoretical capacity

The high electrochemical performance of β-CSe battery anode, including the low equilibrium voltage with good stability, excellent flexibility, and very high theoretical capacity were confirmed through the insertion of Na-ions into both sides of the monolayer and carried out a BHMC [53] search for the global minimum configurations of each concentration. The double-sided adsorption model employed here is standard practice in computational studies of 2D anode materials, as free-standing or weakly-stacked 2D materials expose both surfaces to the electrolyte, enabling Na-ion access to both sides. Importantly, the 2D materials used for comparison in this work (phosphorene, MXenes, graphene) all employ the same double-sided adsorption convention in their original computational studies, ensuring consistent comparison. With the aim of achieving the lowest energy configuration, at least 200 input structures are checked out by allowing Na-ions to select the adsorption sites at both sides of the β-CSe surface, and the derived lowest energy structure are further optimized within a similar energy/strength convergence criterion. The amount of Na-atom inserted on the anode surface ranging between 1- and 18-atoms have been considered within the framework of these computations and to assess the associated insertion potential, the half-cell process used is as follows:

$$(x_2 - x_1)Na + (x_2 - x_1)e^- + Na_{x_1}CSe \rightleftharpoons Na_{x_2}CSe \tag{4}$$

where, x_1 and x_2 refers to the respective concentrations of Na^+ on both sides of β-CSe surface. The maximum sodium content in the anode was established on the basis of two main principles, namely the adsorption energy which must be negative as well as the high-temperature stability of the material within the charge and discharge mechanism. The first factor which describes the energetic stability was investigated through both average adsorption energy and formation energy of each Na-content with respect to the fully sodiated state ($Na_{x_{max}}$@CSe) by means of the formulas:

$$E_{avg} = \frac{E_{(Na)_x@CSe} - E_{CSe} - (xE_{Na})}{x} \tag{5}$$

$$E_f = E_{(Na)_x@CSe} - [\frac{x \cdot E_{Na_{x_{max}}@CSe} + (x_{max} - x)E_{CSe}}{x_{max}}] \tag{6}$$

With x_{max} representing the fully Na^+-concentration. The insertion potential is therefore estimated from the middle-phases appearing in the convex-hull tie line. Hence, the insertion potential (V) can be calculated from the segment of the distinct middle-phases by means of:

$$V = \frac{E_{Na_{x_1}CSe} - E_{Na_{x_2}CSe} + (x_2 - x_1)E_{Na}}{(x_2 - x_1)e} \tag{7}$$

Fig. 4 depicts the formation energies for Na_xCSe configurations, the intermediate configurations showing the smallest formation energies along the hull line are highlighted with black-circles. Then, only these robust structures will be considered for the estimation of the insertion voltage. It can be also observed that the sodium intercalation process can yield fluctuating insertion potentials due to many stable intermediate structures derived. Fig. 5 shows the insertion profile and the average binding energies as a function of Na-concentrations. It can be observed that 10 discharge profile plateaus are obtained with an average insertion profile of 1.11 V.

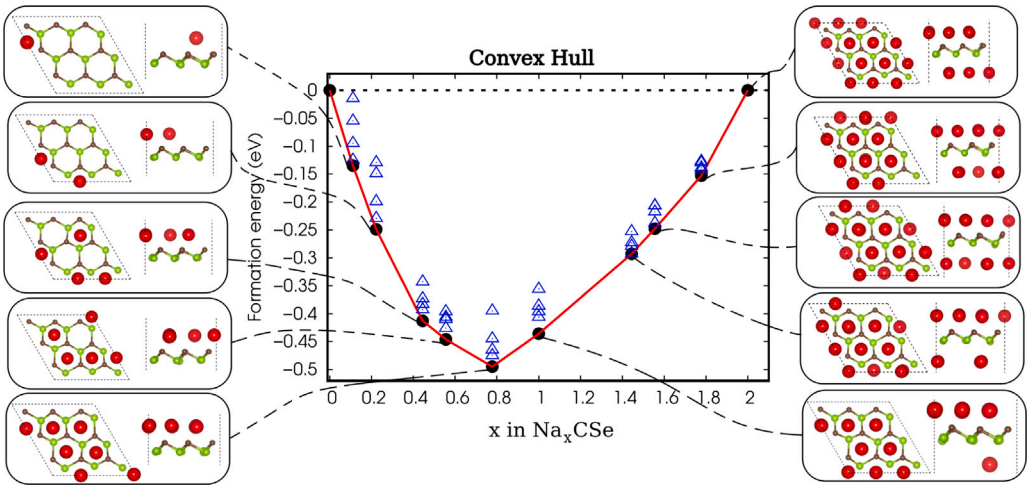

Fig. 4. The formation energies of Na_xCSe with respect to x calculated by taking into account only the ground-state systems obtained by the BHMC with the corresponding global-minimum intermediates structures which appears in the tie-line of the convex-hull. The inset structures show fully relaxed Na-adsorbed configurations at representative concentrations, with Na atoms at their equilibrium positions after geometric optimization.

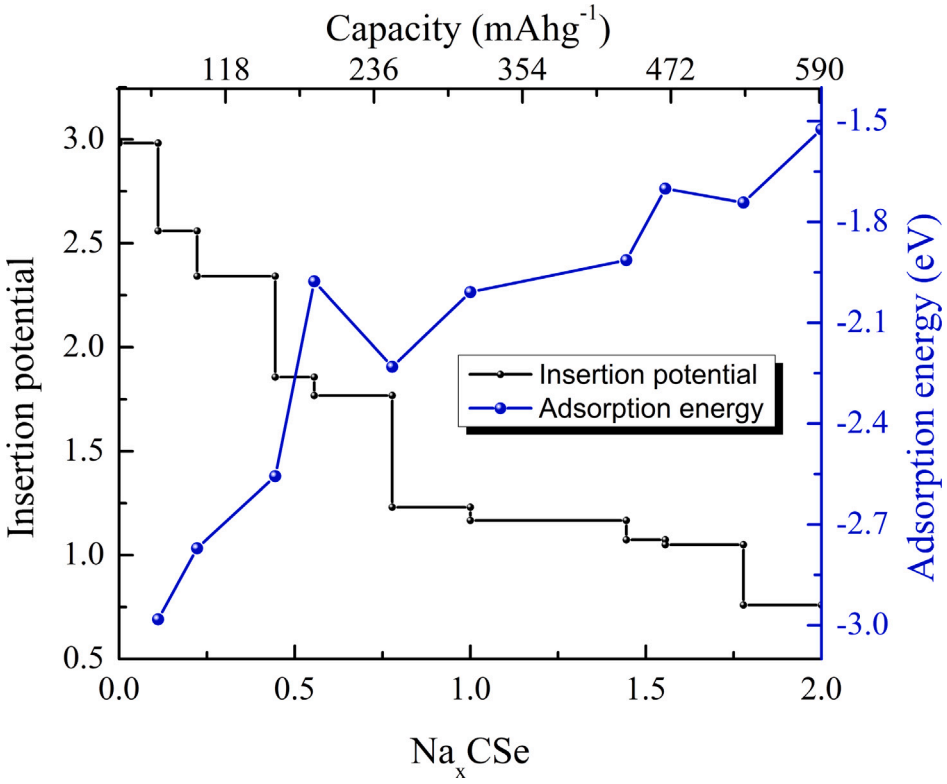

Fig. 5. The insertion profile, adsorption energy and capacity as a function of Na concentrations in pristine CSe monolayer. The red line represents the binding energy and black line displays the insertion profile. The top x-axis shows variation of capacity with increasing Na concentrations.

The non-monotonic behavior in the adsorption energy profile around x = 0.5–0.75 arises from the interplay of several factors: (i) site occupation transition, where at lower concentrations Na atoms preferentially occupy the most favorable hollow sites on the C-side, and as concentration increases, Na atoms begin populating the less favorable Se-side hollow sites, leading to a change in the average binding energy slope; (ii) Na–Na Coulombic interactions, where beyond $x \approx 0.5$, nearest-neighbor Na–Na distances decrease sufficiently that repulsive interactions between the partially charged Na atoms become significant; and (iii) structural relaxation effects, as the β-CSe lattice undergoes gradual expansion with Na loading. This behavior is commonly observed in 2D anode materials and does not indicate instability.

Additionally, the Na^+-insertion storage capacity of the β-CSe anode material is calculated through the formula:

$$C_{th} = \frac{x_{max} \cdot z \cdot F \cdot 10^3}{M_{CSe}} \quad (8)$$

The calculated theoretical Na^+-storage capacity is about 589.22 mAh/g. Such values are considerably greater than the capacity of graphite anode material.

To assess the structural stability during the sodiation process, we examined the evolution of lattice parameters as a function of Na concentration. At maximum sodiation (Na_2CSe), the in-plane lattice constants expand by approximately 3.2%, while the buckling height

increases by about 4.5% relative to pristine β-CSe. These modest structural changes, which are significantly smaller than those observed in conventional anode materials such as silicon (≈300%) or graphite (≈10%), can be attributed to two factors: (i) the inherently buckled structure, which provides accommodation space for Na ions, and (ii) the anisotropic mechanical properties, characterized by an exceptionally low Poisson's ratio of ~0.05 along the armchair direction, which minimizes lateral expansion. The low Poisson's ratio indicates that when the material experiences stress in one direction from Na insertion, it exhibits minimal contraction/expansion in the perpendicular direction. This directional strain decoupling allows the material to locally accommodate Na atoms without propagating strain across the lattice, while the inherent buckling provides out-of-plane accommodation space, working synergistically to minimize in-plane expansion. Such limited volume changes during cycling are highly advantageous for maintaining electrode structural integrity and achieving excellent cycling stability.

To validate the thermal stability of the fully sodiated electrode at operating conditions, we performed AIMD simulations for Na_2CSe at room temperature for 10 ps. The structure exhibits excellent thermal stability with no structural degradation or Na desorption observed. The Na atoms remain at their adsorption sites with normal thermal vibrations, while the C-Se bonds maintain their integrity throughout the simulation. The energy and temperature fluctuations remain within typical equilibrium ranges, confirming the thermal stability of the β-CSe electrode during full charge–discharge cycles at room temperature.

3.4. Diffusion kinetics during sodiation

The further elaboration of advanced and high-efficiency rechargeable Na-ion batteries is critically dependent on the applicability of the negative electrode, notably throughout the processes of charging and discharging which is mainly characterized by both the kinetic properties of dilute Na-ion diffusion as well as electron transfer from Na-atom to the surface. Hence, the electronic behavior of a single and several Na-atoms adsorbed on both sides of β-CSe monolayer were evaluated by computing their density of state as depicted in Fig. 6. It can be clearly seen from our results that our materials shift from semiconductor to metallic characteristic after Na-adsorption on both sides of the system. This transition is evidenced by the finite density of states at the Fermi level and bands crossing the Fermi level in the Na-adsorbed structures, confirming metallic character essential for electronic conductivity during cycling. Thereby providing a fast and efficient exchange of electrons in the electrode during the complete adsorption–desorption cycle, and serves as a major factor in the high-rate capacity of Na-ion based battery.

Additionally, the dilute Na-migration pathways with the corresponding minimum energy profile were investigated by CI-NEB approach for a single Na-atom diffused on the surface of each side of β-CSe system. In Fig. 7, the schematic representative of two Na-scattering pathways considered in our study with their minimum energy are illustrated. The chosen pathways consist of a symmetrical Na-diffusion from the most stable site characterized by the highest binding energy (Hollow site) to another over C/Se-atom on either side of the 2D β-CSe system. Due to the P3m1 space group symmetry of β-CSe, these two pathways represent all symmetry-inequivalent diffusion routes between adjacent hollow sites: Path 1 (H → T_C → H, through top-of-carbon site) and Path 2 (H → T_{Se} → H, through top-of-selenium site). All other pathways are symmetry-equivalent to these two; direct H → H paths without intermediate sites would require Na atoms to pass through the CSe plane, which is energetically prohibitive.

The first pathway involves the Na-atom migrating between two nearest H-sites through the C-atom (i.e., H ↦ T_C ↦ H) on each side of 2D β-CSe system. In this case, it can be clearly noticed from Fig. 7 that the Na-atom needs to exceed a minimum energy profile of 0.408 eV and 0.021 eV to diffuse towards the closest H-site on C- and Se-side of β-CSe monolayer, respectively. For pathway 2, the Na-ion migrates from H-site to neighboring H-site through the top of Se-atom (i.e., H ↦ T_{Se} ↦ H) with a computed minimum barrier profile of 0.019 eV and 0.269 eV with respect to C- and Se-Side of β-CSe system. The CI-NEB calculations reveal that the Na-atom must overcome an energy barrier corresponding to the transition state at the top site when migrating between adjacent hollow sites. For the most favorable diffusion pathway (H → T_{Se} → H on C-side and H → T_C → H on Se-side), the maximum energy barriers are remarkably low at 0.019 eV and 0.021 eV, respectively. These barrier heights represent the energy difference between the stable hollow site configuration and the transition state at the top site, and are among the lowest reported for any 2D anode material.

These outcomes are consistent with the binding energy values; the Na-diffusion barrier is slightly similar between the first pathway on Se-side and the second pathway on C-side of β-CSe material surface. Based on a thorough analysis of these data, it can be stated that our proposed anode material provides fast and efficient Na diffusion. Moreover, comparing these outcomes with alternative battery anodes previously reported in recent literature [12,51,52] provides an even more compelling picture.

To highlight the competitive advantages of β-CSe as a SIB anode, we compare its key performance metrics with other prominent 2D materials reported in literature. The β-CSe monolayer exhibits significantly lower Na diffusion barriers (0.019–0.021 eV) compared to widely studied materials including MXenes such as Ti_3C_2 (0.07–0.19 eV) [54], phosphorene derivatives including black phosphorene (0.04–0.08 eV) and blue phosphorene (0.16 eV), transition metal dichalcogenides like MoS_2 (0.20–0.50 eV), and other carbon-based materials such as graphene (0.28–0.40 eV). The theoretical capacity of 589 mAh/g places β-CSe among the high-capacity candidates, exceeding graphene (~280 mAh/g), black phosphorene (~433 mAh/g), and many MXene compositions (~200–350 mAh/g), while remaining competitive with blue phosphorene (~865 mAh/g) and some high-capacity MXenes. Combined with strong Na binding that thermodynamically favors dispersed Na distribution and favorable insertion potential (1.11 V), β-CSe represents a well-balanced anode material that addresses the key challenges in SIB development.

3.5. Additional comment on the performance of β-CSe during sodiation

The effect of mechanical strain and external electric fields is an effective strategy to modulate the physical/chemical properties of ultrathin nanomaterials [55–57]. The variations of electronic band gap as function of mechanical strain as well as external electric field were investigated. Initially, we have investigated the effect of bi-axial strain on the structural and electronic properties of β-CSe monolayer. When we apply both compressive- and tensile-strains assigned as (+) and (−), respectively. Accordingly, we have systematically studied the strain along its unit-cell. It was seen that the strain is directly measured in terms of variation in lattice constant (Δa). The buckling height and bond-length between C and Se atoms display almost linear variations (see Figure S1(a,b)).

The electronic band structure significantly changes by applying mechanical strain (see Figure S2(a)). The band gap remains almost constant under tensile strain while at compressive strain it displays significant reduction in band gap and shows metallic character above 10%. Furthermore, we have applied the transverse electric field which acts as a staggered potential for the hexagonal atomic arrangement system. We can see that the external electric field modified the electronic band structure of the β-CSe monolayer. We have investigated the calculations by an applied transverse electric field varying from −1 V/Å to +1 V/Å (see Figure S2(b)). It is seen that there is no modification in the electronic band gap for an external electric field ranging from 0 to 1 V/Å. But in case of transverse electric field in the opposite direction then the band gap also not affected up to −0.7 V/Å while above this

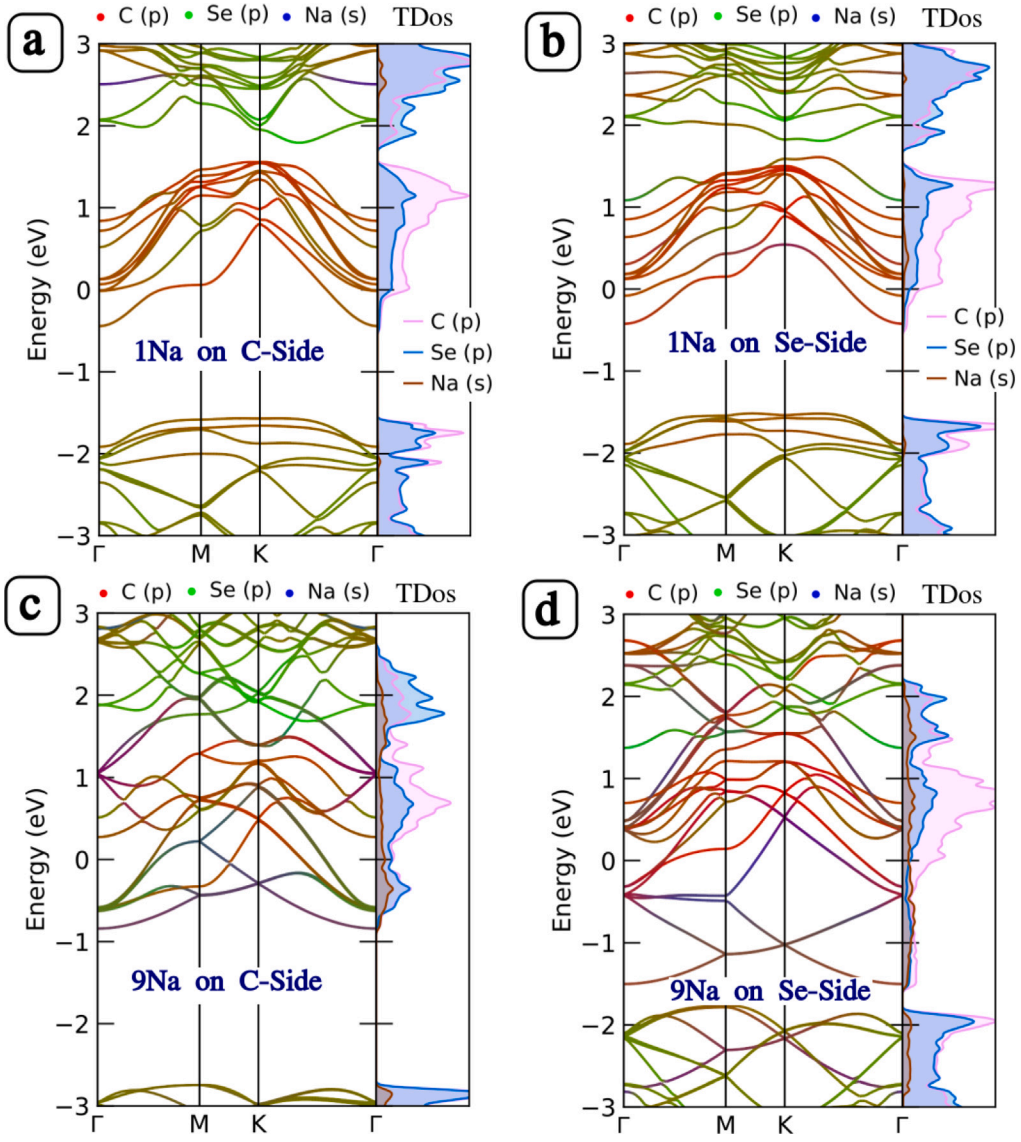

Fig. 6. The electronic projected band structure with corresponding projected density of states after the adsorption of 1Na-atom on C-Side (a), Se-Side (b) of β-CSe monolayer and after 9Na adsorbed on C-Side (c), Se-Side (d) β-CSe monolayer.

electric field strength, the band gap drastically reduced linearly and shows metallic character at −1 V/Å (see Figure S2(b)).

Furthermore, we have systematically investigated the effect of strain when Na atom is adsorbed on the surface of β-CSe monolayer. It is found that the small variation in vertical distance between the Na atom and surface of β-CSe monolayer as shown in Figure S3(a). When Na atom is adsorbed on C-layer side then the maximum charge transfer occurs (see Figure S3(b)) while less charge transfer has been found in case of Se-layer side. The charge transfer varies linearly between Na atom and surface of β-CSe monolayer. The corresponding adsorption energy is significantly influenced on both C-layer and Se-layer side by the applied mechanical strain as depicted in Figure S3(c). It is found that there is no effect of adsorption energy when Na atom is adsorbed on C-layer side of β-CSe monolayer for tensile strain. While in case of compressive strain, the binding energy increases linearly with increasing strain. Similar adsorption energy behavior is found in case of Se-layer side when Na atom is adsorbed but drastic changes in adsorption energy occur with compressive strain.

In addition, we have newly investigated the effect of a uniform electric field on the performance of SIB which uses the β-CSe monolayer as an anode material. When the Na-ions are adsorbed on the C-side of the β-CSe monolayer then the binding energy is significantly stronger in the case of negative electric field strength. While positive electric field is applied then the binding energy weakens slightly as compared to the negative electric field (see Fig. 8). During the negative electric field strength, more electron transfer occurs (~1 electron) as compared to positive electric field due to the Na ions being more polarized with negative electric field. From these results we can say that the Carbon is strongly covalent bonding with Se atom in the β-CSe monolayer. Similarly, when Na ions are adsorbed on the Se side of β-CSe monolayer then opposite trends are found. The positive electric field increased the charge transfer and adsorption energy and the negative electric field has similar adsorption energy and reduced the charge transfer (see Fig. 8).

4. Conclusions

We have demonstrated through comprehensive first-principles calculations that 2D β-CSe monolayer exhibits exceptional potential as an anode material for sodium-ion batteries. The material combines remarkable structural stability (confirmed by phonon spectra and AIMD at both 300 K and 400 K) with ultralow Na^+ diffusion barriers (0.019–0.021 eV), approximately 10–15 times lower than typical 2D anode materials like MXenes (0.2–0.3 eV) and phosphorene derivatives

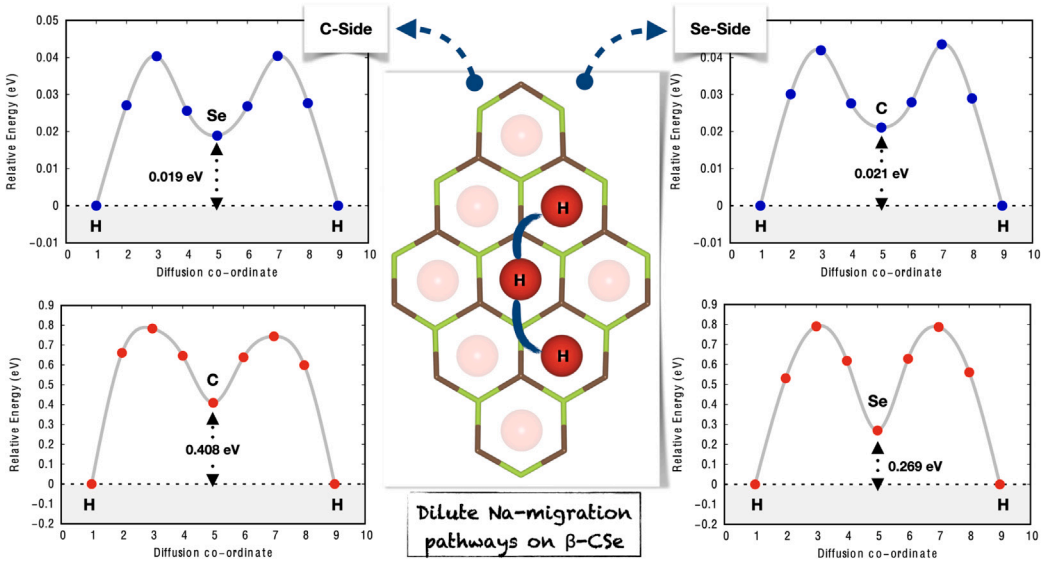

Fig. 7. Schematic illustration of single Na-ion diffusion paths on β-CSe surface and the minimum energy profiles along two optimized paths on both side of β-CSe surface, namely, C- and Se-Side. Path 1 (H → T_C → H) and Path 2 (H → T_{Se} → H) are labeled on both the structural schematic and corresponding energy barrier plots with matching colors for identification.

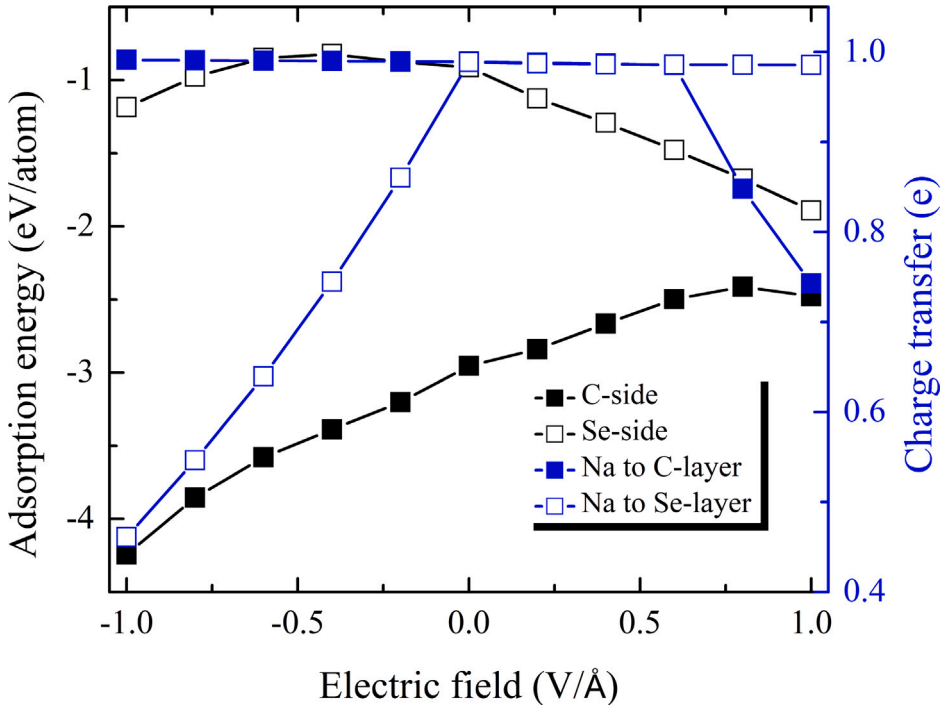

Fig. 8. The variation of adsorption energy as a function of applied external electric field when Na atom is adsorbed on the surface of β-CSe monolayer.

(0.2–0.4 eV). Unlike conventional graphite anodes that suffer from limited Na storage, β-CSe delivers a high theoretical capacity of 589.22 mAh g^{-1} with an average insertion potential of 1.11 V, while maintaining strong Na binding (−2.954 eV on C-side) with substantial charge transfer (0.82|e|) that thermodynamically favors uniform Na distribution, which may help suppress dendrite formation. The material's semiconductor-to-metal transition upon Na adsorption ensures excellent electronic conductivity during cycling, while its anisotropic mechanical properties – particularly the notably low Poisson's ratio of 0.05 along the armchair direction – minimize volume expansion during sodiation. These properties, combined with the ability to tune electrochemical performance through applied electric fields (enhancing binding strength by up to 35% under −1.0 V/Å on C-side), position β-CSe as a promising candidate for next-generation sodium-ion batteries, potentially addressing the critical challenges of capacity, rate capability, and cycle life that currently limit commercial SIB development.

Future work should focus on experimental synthesis and electrochemical testing to validate these computational predictions.

CRediT authorship contribution statement

Talha Zafer: Writing – review & editing, Writing – original draft, Visualization, Software, Methodology. **Deobrat Singh:** Writing – review & editing, Supervision, Formal analysis, Conceptualization.

Declaration of competing interest

The authors declare that they have no known competing financial interests or personal relationships that could have appeared to influence the work reported in this paper.

Acknowledgments

T.Z. acknowledges the computational resources provided by Dutch Research Organization NWO (Snellius@Surfsara) and DelftBlue supercomputer provided by Delft High-Performance Computing Centre (https://www.tudelft.nl/dhpc). DS acknowledges SNIC (2022/22-1230) and NAISS (NAISS 2024/22-1698) Sweden for providing computing facilities.

Appendix A. Supplementary data

Supplementary material related to this article can be found online at https://doi.org/10.1016/j.apsusc.2026.166511.

Data availability

No data was used for the research described in the article.

References

[1] D. Singh, V. Shukla, N. Khossossi, A. Ainane, R. Ahuja, Harnessing the unique properties of MXenes for advanced rechargeable batteries, J. Phys.: Energy 3 (1) (2020) 012005.
[2] N. Khossossi, D. Singh, A. Ainane, R. Ahuja, Recent progress of defect chemistry on 2D materials for advanced battery anodes, Chem. Asian J. 15 (21) (2020) 3390–3404.
[3] A. Manthiram, An outlook on lithium ion battery technology, ACS Central Sci. 3 (10) (2017) 1063–1069.
[4] R.P. Jadav, D. Singh, R. Ahuja, Y. Sonvane, Harnessing MBene termination for superior anode interfaces in Li/Ca-ion batteries, J. Energy Storage 101 (2024) 113995.
[5] X. Zhang, Z. Ju, Y. Zhu, K.J. Takeuchi, E.S. Takeuchi, A.C. Marschilok, G. Yu, Multiscale understanding and architecture design of high energy/power lithium-ion battery electrodes, Adv. Energy Mater. 11 (2) (2021) 2000808.
[6] X. Fan, B. Liu, J. Liu, J. Ding, X. Han, Y. Deng, X. Lv, Y. Xie, B. Chen, W. Hu, et al., Battery technologies for grid-level large-scale electrical energy storage, Trans. Tianjin Univ. 26 (2) (2020) 92–103.
[7] Q. Wu, J. Yang, Y. Zhao, R. Song, Z. Wang, Z. Huang, M. Shi, Y. Ye, D. He, S. Mu, Lifting the energy density of lithium ion batteries using graphite film current collectors, J. Power Sources 455 (2020) 227991.
[8] A. Manthiram, A reflection on lithium-ion battery cathode chemistry, Nat. Commun. 11 (1) (2020) 1–9.
[9] Y. Fang, L. Xiao, Z. Chen, X. Ai, Y. Cao, H. Yang, Recent advances in sodium-ion battery materials, Electrochem. Energy Rev. 1 (3) (2018) 294–323.
[10] Z. Shadike, E. Zhao, Y.-N. Zhou, X. Yu, Y. Yang, E. Hu, S. Bak, L. Gu, X.-Q. Yang, Advanced characterization techniques for sodium-ion battery studies, Adv. Energy Mater. 8 (17) (2018) 1702588.
[11] P.A. Maughan, V.R. Seymour, R. Bernardo-Gavito, D.J. Kelly, S. Shao, S. Tantisriyanurak, R. Dawson, S.J. Haigh, R.J. Young, N. Tapia-Ruiz, et al., Porous silica-pillared MXenes with controllable interlayer distances for long-life Na-ion batteries, Langmuir 36 (16) (2020) 4370–4382.
[12] N. Khossossi, V. Shukla, Y. Benhouria, I. Essaoudi, A. Ainane, R. Ahuja, G. Babu, P.M. Ajayan, Exploring the possibility of β-phase arsenic-phosphorus polymorph monolayer as anode materials for sodium-ion batteries, Adv. Theory Simul. 3 (8) (2020) 2000023.
[13] H. Kim, H. Kim, Z. Ding, M.H. Lee, K. Lim, G. Yoon, K. Kang, Recent progress in electrode materials for sodium-ion batteries, Adv. Energy Mater. 6 (19) (2016) 1600943.
[14] A. Urban, D.-H. Seo, G. Ceder, Computational understanding of Li-ion batteries, Npj Comput. Mater. 2 (2016) 16002, http://dx.doi.org/10.1038/npjcompumats.2016.2.
[15] Q. Bai, L. Yang, H. Chen, Y. Mo, Computational studies of electrode materials in sodium-ion batteries, Adv. Energy Mater. 8 (17) (2018) 1702998.
[16] P.K. Nayak, L. Yang, W. Brehm, P. Adelhelm, From lithium-ion to sodium-ion batteries: Advantages, challenges, and surprises, Angew. Chem. Int. Ed. 57 (1) (2018) 102–120.
[17] C. Yang, S. Xin, L. Mai, Y. You, Materials design for high-safety sodium-ion battery, Adv. Energy Mater. 11 (2) (2021) 2000974.
[18] W. Guo, Z. She, H. Xue, X. Zhang, Density functional theory study on the Ti3CN and Ti3CNT2 (T=O, S and F) as high capacity anode material for Na ion batteries, Appl. Surf. Sci. 529 (2020) 147180.
[19] W. Nong, Y. Li, C. Wang, C3N monolayer with substitutional doping and strain modulation serving as anode material of lithium-ion batteries, Appl. Surf. Sci. 510 (2020) 145324.
[20] S. Jana, S. Thomas, C.H. Lee, B. Jun, S.U. Lee, Rational design of a PC3 monolayer: A high-capacity, rapidly charging anode material for sodium-ion batteries, Carbon 157 (2020) 420–426.
[21] A.P. Durajski, K.M. Gruszka, P. Niegodajew, First-principles study of a substitutionally doped phosphorene as anode material for Na-ion batteries, Appl. Surf. Sci. 532 (2020) 147377.
[22] N.K. Jena, R.B. Araujo, V. Shukla, R. Ahuja, Borophane as a benchmate of graphene: A potential 2D material for anode of Li and Na-ion batteries, ACS Appl. Mater. & Interfaces 9 (19) (2017) 16148–16158.
[23] N. Khossossi, A. Banerjee, I. Essaoudi, A. Ainane, P. Jena, R. Ahuja, Thermodynamics and kinetics of 2D g-GeC monolayer as an anode materials for Li/Na-ion batteries, J. Power Sources 485 (2021) 229318.
[24] G. Abbas, S. Alay-e Abbas, A. Laref, Y. Li, W. Zhang, Two-dimensional B3P monolayer as a superior anode material for Li and Na ion batteries: A first-principles study, Mater. Today Energy 17 (2020) 100486.
[25] Z. Cheng, X. Zhang, H. Zhang, J. Gao, H. Liu, X. Yu, X. Dai, G. Liu, G. Chen, A theoretical prediction of NP monolayer as a promising electrode material for Li-/Na-ion batteries, Appl. Surf. Sci. 547 (2021) 149209.
[26] R.P. Jadav, D. Singh, R. Ahuja, Y. Sonvane, Fluorine-terminated MXene as an anode material for dual-ion (Ca2+/Mg2+) batteries with rapid diffusion mobility, J. Phys. Chem. C 128 (32) (2024) 13539–13549.
[27] X. Wang, S. Kajiyama, H. Iinuma, E. Hosono, S. Oro, I. Moriguchi, M. Okubo, A. Yamada, Pseudocapacitance of MXene nanosheets for high-power sodium-ion hybrid capacitors, Nat. Commun. 6 (1) (2015) 1–6.
[28] M. Mayo, K.J. Griffith, C.J. Pickard, A.J. Morris, Ab initio study of phosphorus anodes for lithium-and sodium-ion batteries, Chem. Mater. 28 (7) (2016) 2011–2021.
[29] N. Khossossi, A. Banerjee, Y. Benhouria, I. Essaoudi, A. Ainane, R. Ahuja, Ab initio study of a 2D h-BAs monolayer: A promising anode material for alkali-metal ion batteries, Phys. Chem. Chem. Phys. 21 (33) (2019) 18328–18337.
[30] Z. Ma, B. Wang, L. Ou, Y. Zhang, X. Zhang, Z. Zhou, Structure and properties of phosphorene-like IV-VI 2D materials, Nanotechnology 27 (41) (2016) 415203.
[31] M. Batmunkh, M. Bat-Erdene, J.G. Shapter, Phosphorene and phosphorene-based materials–prospects for future applications, Adv. Mater. 28 (39) (2016) 8586–8617.
[32] S. Karmakar, C. Chowdhury, A. Datta, Two-dimensional group IV monochalcogenides: Anode materials for Li-ion batteries, J. Phys. Chem. C 120 (27) (2016) 14522–14530.
[33] H. Jiang, T. Zhao, Y. Ren, R. Zhang, M. Wu, Ab initio prediction and characterization of phosphorene-like SiS and SiSe as anode materials for sodium-ion batteries, Sci. Bull. 62 (8) (2017) 572–578.
[34] F. Wang, Q. Yao, L. Zhou, Z. Ma, M. He, F. Wu, Theoretical understanding of SnS monolayer as Li ion battery anode material, J. Phys. Chem. Solids 121 (2018) 261–265.
[35] Y. Zhou, M. Zhao, Z.W. Chen, X.M. Shi, Q. Jiang, Potential application of 2D monolayer β-GeSe as an anode material in Na/K ion batteries, Phys. Chem. Chem. Phys. 20 (48) (2018) 30290–30296.
[36] G. Kresse, J. Furthmüller, Efficient iterative schemes for ab initio total-energy calculations using a plane-wave basis set, Phys. Rev. B 54 (16) (1996) 11169.
[37] J.P. Perdew, K. Burke, M. Ernzerhof, Generalized gradient approximation made simple, Phys. Rev. Lett. 77 (18) (1996) 3865.
[38] J. Heyd, G.E. Scuseria, M. Ernzerhof, Hybrid functionals based on a screened Coulomb potential, J. Chem. Phys. 118 (18) (2003) 8207–8215.
[39] H.J. Monkhorst, J.D. Pack, Special points for Brillouin-zone integrations, Phys. Rev. B 13 (12) (1976) 5188.
[40] G. Henkelman, A. Arnaldsson, H. Jónsson, A fast and robust algorithm for bader decomposition of charge density, Comput. Mater. Sci. 36 (3) (2006) 354–360.
[41] M. Parrinello, A. Rahman, Crystal structure and pair potentials: A molecular-dynamics study, Phys. Rev. Lett. 45 (14) (1980) 1196.
[42] L. Kantorovich, N. Rompotis, Generalized Langevin equation for solids. II. Stochastic boundary conditions for nonequilibrium molecular dynamics simulations, Phys. Rev. B 78 (9) (2008) 094305.
[43] G. Henkelman, B.P. Uberuaga, H. Jónsson, A climbing image nudged elastic band method for finding saddle points and minimum energy paths, J. Chem. Phys. 113 (22) (2000) 9901–9904.
[44] B. Lv, X. Hu, X. Liu, Z. Zhang, J. Song, Z. Luo, Z. Gao, Thermal transport properties of novel two-dimensional CSe, Phys. Chem. Chem. Phys. 22 (32) (2020) 17833–17841.
[45] S. Li, M. Shi, J. Yu, S. Li, S. Lei, L. Lin, J. Wang, Two-dimensional blue-phase CX (X=S, Se) monolayers with high carrier mobility and tunable photocatalytic water splitting capability, Chin. Chem. Lett. 32 (6) (2021) 1977–1982.

[46] Q. Zhang, Y. Feng, X. Chen, W. Zhang, L. Wu, Y. Wang, Designing a novel monolayer β-CSe for high performance photovoltaic device: An isoelectronic counterpart of blue phosphorene, Nanomaterials 9 (4) (2019) 598.
[47] Z. Zhu, D. Tománek, Semiconducting layered blue phosphorus: A computational study, Phys. Rev. Lett. 112 (17) (2014) 176802.
[48] W. Zhang, H. Enriquez, Y. Tong, et al., Epitaxial synthesis of blue phosphorene, Small 14 (2018) 1804066, http://dx.doi.org/10.1002/smll.201804066.
[49] P. Vogt, P. De Padova, C. Quaresima, et al., Silicene: Compelling experimental evidence for graphenelike two-dimensional silicon, Phys. Rev. Lett. 108 (2012) 155501, http://dx.doi.org/10.1103/PhysRevLett.108.155501.
[50] N. Khossossi, Y. Benhouria, S.R. Naqvi, P.K. Panda, I. Essaoudi, A. Ainane, R. Ahuja, Hydrogen storage characteristics of li and Na decorated 2D boron phosphide, Sustain. Energy & Fuels 4 (9) (2020) 4538–4546.
[51] H. Jiang, W. Shyy, M. Liu, L. Wei, M. Wu, T. Zhao, Boron phosphide monolayer as a potential anode material for alkali metal-based batteries, J. Mater. Chem. A 5 (2) (2017) 672–679.
[52] S. Wang, W. Zhang, C. Lu, Y. Ding, J. Yin, P. Zhang, Y. Jiang, Enhanced ion diffusion induced by structural transition of Li-modified borophosphene, Phys. Chem. Chem. Phys. 22 (37) (2020) 21326–21333.
[53] D.J. Wales, H.A. Scheraga, Global optimization of clusters, crystals, and biomolecules, Science 285 (5432) (1999) 1368–1372.
[54] Q. Tang, Z. Zhou, P. Shen, Are MXenes promising anode materials for Li ion batteries? Computational studies on electronic properties and li storage capability of Ti3C2 and Ti3C2X2 (X=F, OH) monolayer, J. Am. Chem. Soc. 134 (2012) 16909–16916, http://dx.doi.org/10.1021/ja308463r.
[55] C. Kamal, M. Ezawa, Arsenene: Two-dimensional buckled and puckered honeycomb arsenic systems, Phys. Rev. B 91 (8) (2015) 085423.
[56] D. Singh, N. Khossossi, A. Ainane, R. Ahuja, Modulation of 2D GaS/BTe vdw heterostructure as an efficient HER catalyst under external electric field influence, Catal. Today (2020).
[57] D. Singh, S.K. Gupta, Y. Sonvane, T. Hussain, R. Ahuja, Achieving ultrahigh carrier mobilities and opening the band gap in two-dimensional Si 2 BN, Phys. Chem. Chem. Phys. 20 (33) (2018) 21716–21723.